Characterization and Validation of R410A Condensation Performance in Split Air Conditioning Units: Experimental Investigation and ANSYS Fluent Simulation

Veyan A. Musa [1,2,*], Omar M. Ali [1], and Raid A. Mahmood [1]

[1] Department of Mechanical Engineering, University of Zakho, Zakho, Iraq
[2] Engineering Research Center, University of Zakho, Zakho, Iraq
Email: veyan.musa@uoz.edu.krd (V.A.M.); Omar.ali@uoz.edu.krd (O.M.A.); raid.ahmed@uoz.edu.krd (R.A.M.)
*Corresponding author

***Abstract*—This study presents a thorough characterization and validation of R410A condensation performance in split air conditioning units, offering actionable insights for industry and addressing the critical challenges of energy efficiency and climate adaptation in regions such as the Kurdistan Region of Iraq. By integrating advanced experimental instrumentation with high-fidelity Computational Fluid Dynamics (CFD) modeling, it presents a comprehensive investigation of two-phase flow dynamics across the full length of an 8.914 m copper condenser tube. Forty-one precisely calibrated temperature sensors and pressure transducers provide real monitoring of thermal and flow behavior. The Volume of Fluid (VOF) method with geometric reconstruction and level set interface tracking was implemented for CFD modeling, providing direct visualization of evolving refrigerant flow patterns. Distinct flow regimes were identified: a fully vapor, desuperheating region near the inlet (0–1.8 m), a condensation zone (1.8–6 m) marked by classic stratified and annular two-phase flow with a sharp decline in vapor void fraction and a near-constant temperature and a subcooled liquid zone (6–8.9 m) where the tube was completely filled with liquid. The presence and length of each regime were confirmed by 2D cross-sectional CFD images and experimental surface temperature profiles. Pointwise comparison of measured and simulated wall temperatures across all 41 positions yielded a Mean Absolute Error (MAE) of 1.46 °C and a Root Mean Square Error (RMSE) of 1.63 °C, validating the numerical approach. These findings demonstrate that the spatially resolved CFD model captures both the thermal and hydrodynamic developments throughout condensation, supporting more robust and energy-efficient condenser designs for the local operation.**

***Keywords*—R410A condensation, two-phase flow, vapor void fraction, experimental validation**

I. Introduction

Vapor Compression Refrigeration systems (VCRs) are widely used in residential, commercial, and industrial applications, with air conditioning representing their most common use [1]. These systems leverage the thermodynamic properties of refrigerants to absorb heat during evaporation and release it during condensation [2]. The efficiency and reliability of such systems depend critically on the design and performance of their heat exchangers, particularly the condenser, where two-phase flow of refrigerant plays a central role. The interplay between liquid and vapor phases within the tubes is governed by momentum, geometry, mass flow rate, and energy exchange, and directly impacts system performance and energy consumption [3–5]. Recognizing and optimizing the flow structures and patterns of two-phase liquid-vapor flow within condensers is therefore essential for improving overall system efficiency [6].

Despite extensive research into general condenser operation, critical gaps remain in understanding and characterization local condensation performance in real world split air conditioning units under practical operating conditions. Notably, there is a shortage of studies providing spatially resolved experimental data and detailed Computational Fluid Dynamics (CFD) validation that capture the full evolution of two-phase flow regimes, vapor void fraction, and local phase transitions, especially within compact, small diameter tube geometries under regionally relevant climates and operating with modern refrigerants such as R410A. Many existing flow regime maps and predictive models fall short of accurately describing condensation behavior under these conditions, particularly for horizontal tubes commonly used in contemporary split Air Conditioning (AC) condensers [7, 8].

Motivated by these challenges, this study proposes an integrated experimental and computational approach to address the identified gap. By instrumenting an 8.914 m copper condenser tube (5 mm ID) with forty-one precisely calibrated temperature sensors and pressure transducers,

Manuscript received July 4, 2025; revised July 23, 2025; accepted July 31, 2025; published November 14, 2025.

we capture high resolution spatial and temporal data on thermal and flow dynamics relevant to two-phase condensation. In parallel, advanced CFD simulations using the Volume of Fluid (VOF) method with geometric reconstruction and level set interface tracking are applied to predict local phase distributions and vapor void fraction throughout the condenser tube. This approach enables robust validation and provides new insight into local condensation regimes and transitions, under realistic operating conditions typical for the Kurdistan Region of Iraq and similar climates.

By covering the entire outdoor condenser, including all tube sections and fittings the study yields a comprehensive, system level understanding of R410A condensation behavior in split AC units. The findings directly inform condenser design, tube length selection, and guiding principles for adaptation to harsher climates, thus offering practical, actionable recommendations for air conditioning manufacturers and system designers seeking enhanced performance and climate resilience.

II. Literature Review

Recent research has made considerable progress in understanding and modeling two-phase flow and heat transfer in air conditioning systems. Fei *et al.* [9] investigated the boiling heat transfer of R410A outside horizontal tubes using Ansys Fluent, highlighting the impact of mass flow rate and heat flux on heat transfer coefficients. Their simulations, validated against experimental data (<15% discrepancy), provide insights for condenser optimization. Yang *et al.* [10] compared R410A performance in micro fin versus smooth tubes, demonstrating that micro fin tubes offer 3.5–3.6 higher heat transfer capacity. Zou and Hrnjak [11] simulated R410A two-phase flow in vertical headers, revealing flow maldistribution mechanisms critical for header design. Mahmood *et al.* [12] analyzed R134a flow in horizontal pipes, emphasizing the influence of inlet conditions on phase separation. Mancin *et al.* [13] experimentally investigated the condensation of R410A in three different commercial brazed plate heat exchangers, focusing on the effects of mass flow rate and outlet vapor quality on heat transfer performance. Their experiments were conducted at a saturation temperature of 36.5 °C, with mass flow rates ranging from 15 to 40 kg/m².s and outlet vapor qualities between 0.01 and 0.52. This study also compared experimental data with literature models and proposed a new computational procedure for plate heat exchanger design, highlighting the importance of accurate experimental validation for optimizing condenser performance.

III. Experiment Description

This study investigates the condensation dynamics of R410A two-phase flow in the outdoor condenser section of a split air conditioning system with a capacity of 18,000 BTU/hr (full specifications provided in Table I), utilizing advanced sensors and monitoring instruments. The condenser inlet is divided into six asymmetrical sections at its start, which converge at the outlet. Temperature distributions are examined by focusing on a single representative section.

Fig. 1 overviewed the split air conditioning system used in this study. Major components, including compressor, condenser coil, expansion device, and indoor evaporator are indicated. The direction of refrigerant flow is shown by arrows. All measurement points for temperature and pressure sensors are marked with location labels. Fig. 2 detailed the schematic of condenser tube layout with DS18B20 temperature sensors installed at uniform 0.23 m intervals (1–41) from tube inlet to outlet. Pressure sensor placements are also indicated. Arrows show refrigerant flow direction. This arrangement provides high spatial resolution for monitoring temperature variations along the entire condenser length.

Fig. 3 photographed the laboratory experimental setup. The condenser coil, temperature and pressure sensor wiring, data acquisition system (Arduino MEGA 2560), and cooling fan arrangement are labeled for reference. The precise location of each sensor ensures detailed tracking of thermal gradients and supports accurate validation of the heat transfer processes under investigation. These sensors are attached to the outer surface of the copper tube (5 mm internal diameter, 0.5 mm wall thickness) using thermal adhesive, and each sensor is subsequently covered with insulating epoxy to minimize environmental influences. Direct insertion of sensors into the tube for measuring average fluid temperature was impractical due to physical constraints. Three additional sensors monitor refrigerant temperatures at the evaporator inlet, evaporator outlet, and compressor outlet, while an outdoor sensor records ambient conditions (sensors 42–44).

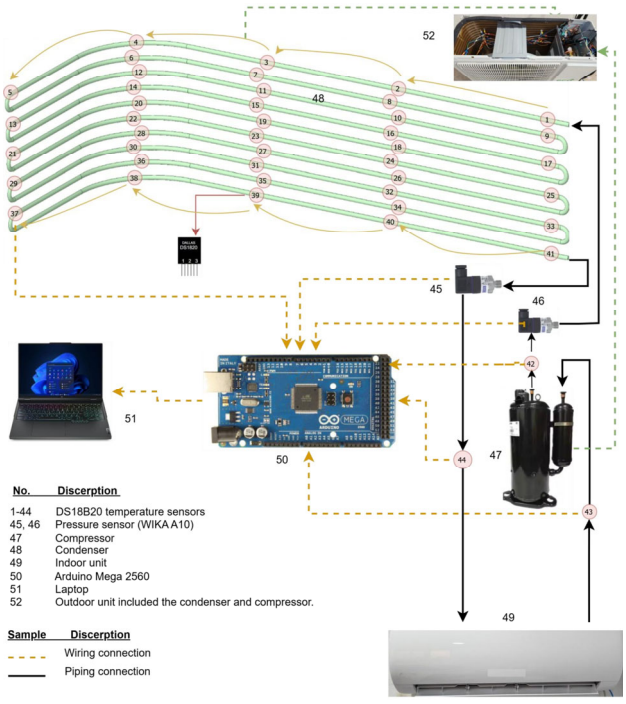

Fig. 1. Schematic/system overview.

TABLE I. THE TECHNICAL SPECIFICATIONS OF 18,000 BTU/HR OF WALL SPLIT

Parameter		Unit	Value
Working Fluid	Fluid	-	R410A
Power Supply	Cooling Capacity	Watt	5275
	Air Flow Volume	m^3/h	850/780/650/580/550
Indoor Unit	Set Temperature Range for Indoor	°C	16～30
Outdoor Unit	Compressor type	-	Rotary, QXAH-E21F050
	Compressor Power Input	W	1690
	Outdoor Unit Air Flow Volume	m^3/h	3000
	Condenser Pipe Diameter	mm	5
	Cooling Operation Ambient Temperature Range	°C	18～52
	Refrigerant Charge	kg	1.1

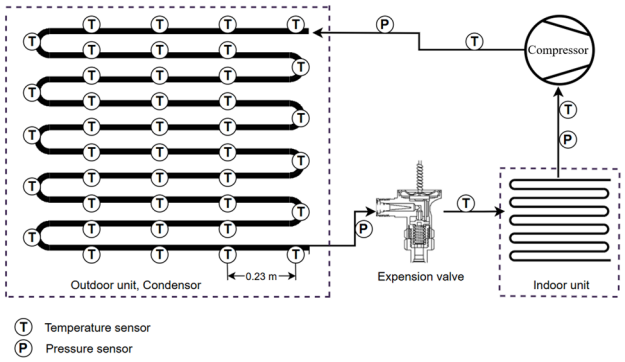

Fig. 2. The system schematic diagram.

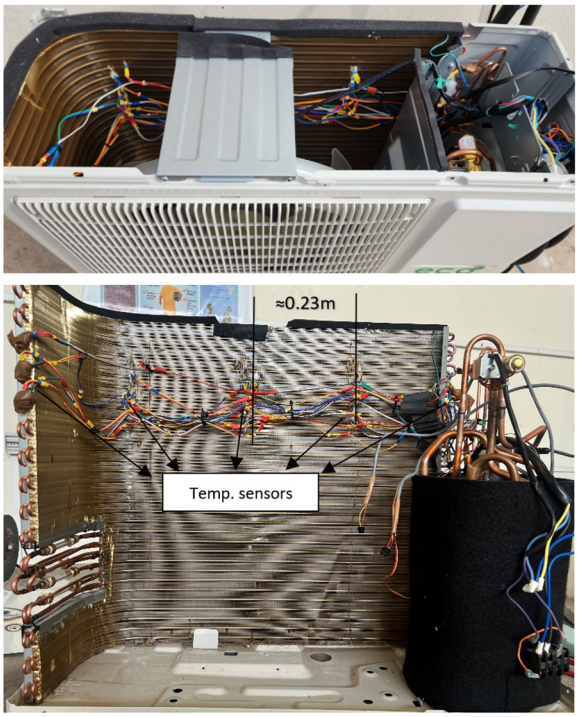

Fig. 3. Temperature sensors distribution along the condenser.

In addition, high accuracy WIKA pressure transducers are installed at both the inlet and outlet of the condenser to capture the pressure drop across the tube, with all measurement signals routed to an Arduino Mega 2560 controller, connected to a laptop for data logging and analysis. To ensure the reliability of the experimental data, a thorough calibration and uncertainty analysis of all sensors was performed. The accuracy specifications of the DS18B20 temperature sensors and the WIKA pressure sensors are summarized in Table II and Table III, respectively. Fig. 4 shows the calibration results a DS18B20 (x-axis) temperature sensor with a RTD PT100 sensor (y-axis) at the operational temperatures ranged (10–80 °C). The line of perfect agreement is shown. The DS18B20 sensors, boasting an accuracy of ±0.5% °C within the measurement range relevant to this study, were regularly cross validated against a high precision RTD PT100 sensor (MP82810 S-Products, ±0.02 °C accuracy) across 18.9 °C to 100.2 °C. Testing at ice/boiling points and intermediate temperatures (18 °C, 28 °C, and 98 °C) revealed a linear correlation, as shown in Fig. 4.

TABLE II. DS18B20 ACCURACY AND SPECS

Specification	Description
Operating Range	−55 °C to + 125 °C
Accuracy	±0.5 °C % (from −10 °C to +85 °C)
Output Resolution	9-bit to 12-bit programmable
Communication	1-Wire bus

TABLE III. WIKA A-10 PRESSURE SENSOR SPECS

Specification	Description
Pressure Range	34 bars
Accuracy	±0.25%
Output Signals	4–20 mA, 0–10 V, or 0–5 V DC
Response Time	Less than 4 ms

All photographs in Figs. 1 and 3 were captured by the authors during the experimental work conducted at the University of Zakho, College of Engineering, as part of this research. This setup provides precise insights into refrigerant flow, thermal behavior, and environmental impacts, aiding efforts to optimize cooling efficiency and energy use in split AC systems under demanding conditions.

The mass flow rate ṁ is determined theoretically using Eq. (1), which employs the energy conservation equation and enthalpy values:

$$\dot{m} = \frac{\eta \dot{W}_{comp}}{h2-h1} \quad (1)$$

Here $\dot{W}_{comp}$ is the compressor power input in W, η is the isentropic thermal efficiency of the compressor, $h1$ and h2 are the specific enthalpies for the compressor outlet and inlet (kJ/kg).

R410A was selected for this study because it is the most widely adopted refrigerant in modern split air conditioning units in the Kurdistan Region of Iraq and globally, particularly for systems installed over the past decade. Its key merits include a zero Ozone Depletion Potential (ODP = 0), high cooling capacity, favorable thermophysical properties (such as high latent heat and moderate operating pressures), and compatibility with existing system components. R410A also offers excellent stability and safety in terms of flammability limits (classified as A1: non-toxic, non-flammable). However, R410A has notable demerits: it possesses a relatively high global warming potential (GWP ≈ 2088), which has prompted recent regulatory and environmental concerns regarding long-term sustainability. In addition, R410A requires higher design and operating pressures compared to older refrigerants (e.g., R22), demanding careful equipment specification and maintenance to ensure safety and efficiency.

All readings are recorded at an outdoor temperature of 29.5 °C, while indoor temperatures ranged from 16 °C to 20 °C. The 18000 BTU split unit is operated, and temperature sensor data were collected along the condenser tube, as well as at the evaporator inlet/outlet and compressor inlet/outlet. Pressure readings are also recorded and stored in an Excel spreadsheet. Test runs are categorized based on the average evaporator saturated temperatures, which were measured at 5.6 °C and 3.1 °C.

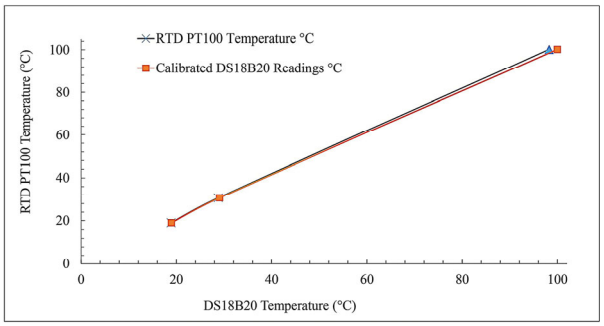

Fig. 4. Calibration of the DS18B20 sensor with RTD PT100.

IV. CFD Modeling

A To thoroughly understand vapor-liquid two-phase flow in pipelines, it is essential to examine how major factors affect phase distributions, and overall flow behavior. While experimental studies often fall short in fully capturing flow patterns, numerical simulation methods play a vital role by complementing experimental research and offering deeper and system wide insights. This section provides a clear overview of the simulation process, detailing the CFD approach and its application to pipeline flows. It explains the numerical methods, governing equations, modeling assumptions, and the setup of initial and boundary conditions. Additionally, the discussion covers computational settings, mesh generation, grid independence checks, and thorough validation steps. By addressing these aspects, the groundwork is established for robust CFD modeling, effectively linking theoretical predictions with practical experimental findings in the study of vapor-liquid flow dynamics.

A. Modeling of Multiphase Flow

For this investigation, the VOF method coupled with level set interface tracking to simulate two-phase flow dynamics. Within this approach, each phase is treated as a continuous medium, and the interface between them is accurately traced by the VOF method. By solving a transport equation that determines the volume fraction of each phase within every computational cell, the method enables precise tracking and representation of the phases' distribution throughout the flow domain. The continuity equation (Eq. (2)) governs mass conservation, while the momentum equation (Eq. (3)) describes fluid motion with shared velocity fields across phases [9].

$$\frac{\partial \rho}{\partial t} + \nabla \cdot (\rho U) = 0 \tag{2}$$

$$\frac{\partial}{\partial t}(\rho U) + \nabla \cdot (\rho U U) = -\nabla \mathrm{p} + \nabla \cdot \tau + \rho g + F \tag{3}$$

where ρ represents density, t denotes time, U is the velocity vector, p is pressure, τ represents the stress tensor, g is the gravitational acceleration vector, and the F symbol stand for density, velocity, viscosity, pressure, gravitational acceleration, and additional body forces such as surface tension respectively. The effective viscosity and density used in the governing equations as mentioned above are determined by averaging the properties of each phase according to their respective volume fractions within the computational domain (Eqs. (4) and (5)).

$$\mu = \sum_1^p \mu_q \alpha_q \tag{4}$$

$$\rho = \sum_1^p \rho_q \alpha_q \tag{5}$$

The phase fraction, denoted by α, quantifies the proportion of each phase within the system and μ is the dynamic viscosity. To model the phase fraction behavior, Eq. (6) represents a specialized continuity equation that governs the temporal and spatial evolution of volume fractions for individual phases. Within every computational cell, Eq. (7) must be consistently satisfied.

$$\frac{\partial \alpha_q}{\partial t} + (\mathrm{U}_q \cdot \Delta) = 0 \tag{6}$$

$$\sum_1^p \alpha_q = 1 \tag{7}$$

Here, the number of phases is denoted by p, while α_q represents the volume fraction of the qth fluid within a computational cell. The volume fraction can exist in three distinct states:

- When α_q = 0, the cell contains none of fluid q.

- If $\alpha_q = 1$, the cell is completely filled with fluid q.
- For $0 < \alpha_q < 1$, the cell contains an interface between fluid q and one or more other fluids.

The VOF method implements a piecewise-linear interface reconstruction technique, modeling the phase boundary as a straight line within each computational cell. This approach calculates fluid advection across cell faces through three sequential steps: First, the interface position relative to the cell center is determined using the local volume fraction and its spatial derivatives. Second, advection fluxes are computed by applying this linear interface representation while incorporating normal and tangential velocity distributions at cell faces. Finally, volume fractions are updated based on the net flux balance derived from these calculations [14].

B. Wall Adhesion and Surface Tension

The VOF method accounts for surface tension by introducing a source term in the momentum equation. This implementation follows the Continuous Surface Force (CSF) model derived by Brackbill *et al.* [15], which incorporates the Young-Laplace equation under the assumption of constant interfacial tension between phases. For vapor-liquid, this yields the formulation in Eq. (8):

$$F = \frac{\sigma(\rho_{\kappa}\nabla\alpha_v)}{0.5\rho_v + 0.5\rho_l} \tag{8}$$

where: ρ_l and ρ_v are the densities of liquid and vapor, α_v is vapor void fraction, σ is surface tension, ρ is the average density of phases (Eq. (5)), and κ is the surface curvature (describes how a surface deviate from being flat). The calculation of surface curvature relies on analyzing local gradients of the surface normal at the interface. This approach provides a detailed representation of the interface geometry, a base for accurately modeling multiphase flows. The normal surface, referred to as n, plays a pivotal role in this calculation. It is defined mathematically in Eq. (9) and Eq. (10) as the gradient of the volume fraction α_v:

$$\kappa = \nabla \cdot \hat{n} \tag{9}$$

$$\hat{n} = \frac{n}{|n|} \tag{10}$$

Wall adhesion effects are directly incorporated into the model through the contact angle at fluid-wall interfaces, defined as a dynamic boundary condition. This inclusion modifies the interfacial curvature near solid boundaries.

$$\hat{n} = \hat{n}_w cos\varphi + \hat{t}_w sin\varphi \tag{11}$$

In Eq. (11), the symbols $\hat{n}_w$ and $\hat{t}_w$ correspond to the unit vectors aligned normal and tangential to the pipe wall. The contact angle, φ, describes the angle formed where the fluid interface meets the wall, measured between the pipe wall and the local tangent to the fluid surface.

C. Turbulence Modeling

Accurate simulation of vapor-liquid flow requires a turbulence model that maintains precision across diverse conditions. The *k-ω* Shear Stress Transport (SST) model addresses this need by solving transport equations for turbulent kinetic energy (k) and specific dissipation rate (ω) as stated in Eqs. (12) and (13). Its core strength lies in a blending function that seamlessly integrates the standard *k-ε* model for bulk flow with the Speziale-Saffman formulation for near wall viscous effects. This hybrid approach delivers three key advantages for vapor-liquid flow systems: enhanced prediction of flow patterns and phase separation, robust performance in complex geometries, and adaptability to varying oil velocities and properties. Particularly valuable for this study, which spans a broad range of liquid viscosities and velocities the model's low-Reynolds formulation maintains accuracy even in laminar flow regions, ensuring reliable predictions across all flow regimes [16].

$$\frac{\partial}{\partial t}(k\rho) + \frac{\partial}{\partial x_j}(k\rho u_j) = \frac{\partial}{\partial x_j}\left[\left(\mu + \frac{\mu_t}{\sigma_k}\right)\frac{\partial k}{\partial x_j}\right] + G_k - Y_k + S_k \tag{12}$$

$$\frac{\partial}{\partial t}(\omega\rho) + \frac{\partial}{\partial x_j}(k\omega u_j) = \frac{\partial}{\partial x_j}\left[\left(\mu + \frac{\mu_t}{\sigma_\omega}\right)\frac{\partial \omega}{\partial x_j}\right] + G_\omega - Y_\omega + S_\omega \tag{13}$$

Here k is the turbulent kinetic energy, u_j is the velocity component in the j-direction μ_t is the turbulent viscosity, σ_k and σ_ω are the turbulent Prandtl numbers for k and ω, G_k represents the generation of turbulent kinetic energy due to mean velocity gradients. G_ω represents the generation of ω, Y_k and Y_ω represent the dissipation of k and ω due to turbulence, and S_k and S_ω are user-defined source terms. $\left(\mu + \frac{\mu_t}{\sigma_k}\right)$ and $\left(\mu + \frac{\mu_t}{\sigma_\omega}\right)$ show the influence diffusivity of k and ω. These equations describe the transport of k and ω in a fluid flow. The left-hand side of each equation represents the rate of change and convection of the respective quantity. The right-hand side includes terms for diffusion, production, dissipation, and any additional source terms. For a comprehensive derivation and deeper theoretical background, reference [17, 18] as well as the Ansys Fluent theoretical guide [19] are included more details.

D. Initial and Boundary Conditions

Drawing on established methodologies in Refs. [20, 21], the simulation initializes with the condenser section (Fig. 5) entirely filled with vapor at t = 0. Superheated R410A vapor (properties in Table IV [22]) enters at 45.3 °C and 21 bar gauge pressure with a constant uniform mass flow rate of 0.0028 kg/s. Condensation occurs along the 8.914 m tube (5 mm internal diameter) at a saturated temperature of 35.3 °C, with ambient temperature maintained at 30 °C, resulting in liquid-phase

exit flow. The pressure outlet boundary condition is justified by negligible flow gradients at the fully developed outlet. No-slip conditions are enforced on all walls.

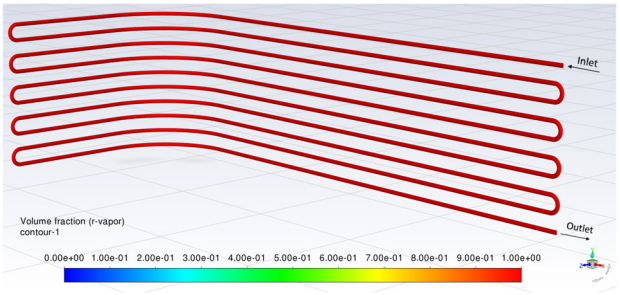

Fig. 5. Condenser configuration with inlet and outlet.

Table IV stated the thermophysical properties of R410A at reference conditions, including boiling point, vapor pressure, ODP, GWP, and safety classification. Data sourced from ASHRAE and manufacturer datasheets.

TABLE IV. THE ESSENTIAL THERMODYNAMICS AND PHYSICAL PROPERTIES OF R410A REFRIGERANT AT 35 °C

Parameter (Unit)	Value
Liquid density (kg/m³)	1020–1030
Vapor density (kg/m³)	~43.6
Liquid viscosity (Pa·s)	~0.00012
Vapor viscosity (Pa·s)	~0.000013
Critical temperature (°C)	72.13
Critical pressure (kPa)	4926.1
Critical volume (m³/kg)	0.00205
Boiling point at 1 atm (°C)	−51.58
Specific heat capacity, liquid (J/kg·K)	~1700–1800
Thermal conductivity, liquid (W/m·K)	~0.089
Ozone depletion potential (ODP)	0
Global warming potential (GWP)	2088

E. Computational Method

The study employs a VOF method coupled with level set interface tracking to simulate condensation dynamics of refrigerant R410A, in 5 mm copper tubes. Simulations in ANSYS Fluent R2 2024 use a 3D transient solver with double precision. Discretization employs second order upwind schemes for momentum/turbulence, PRESTO! for pressure, and geometric reconstruction for VOF.

Volume of Fluid (VOF) and level set method was selected due to its enhanced ability to precisely capture and track vapor-liquid interfaces under dynamic flow conditions. While the standard VOF model effectively handles the conservation of fluid phases and accommodates complex interface deformations, it can sometimes introduce inaccuracies in resolving the sharpness and curvature of the phase boundaries particularly in the states where surface tension and interface topology are critical, as seen in condensation within heat exchanger tubes. By coupling the VOF approach with the level set method, which maintains a sharp and smooth representation of the interface and delivers more accurate curvature calculations, the simulation achieves both mass conservation and high-fidelity interface tracking. This hybrid technique results in more reliable predictions of local phase distribution, vapor void fraction, and temperature gradients, all of which were confirmed through detailed comparisons with experimental measurements. The effectiveness of this combined methodology for multiphase flows with phase change and surface tension effects is well supported in the literature, including by Alsehli *et al.* [16], they demonstrated its advantages in capturing free-surface dynamics in complex fluid systems.

An equivalent coefficient h_{eq} in Eq. (14) simplifies finned condenser modelling by combining base convection h utilizing the Nusselt Nu correlation Eq. (15) with fin efficiency η and area ratios. This approach aligns with experimental data for R410A condensation in 5 mm tubes, validating interfacial heat transfer predictions [23].

$$h_{eq} = h \times \frac{A_{base}}{A_{total}} \times \eta \tag{14}$$

$$Nu = C \times Re^{m} \times Pr^{n} \tag{15}$$

In this study, the treatment of external heat transfer from the condenser tube wall to the surrounding air was addressed using an equivalent natural convection heat transfer coefficient, h_{eq} within the ANSYS Fluent simulation. Instead of modeling the detailed forced air convective environment with the actual fins, a representative h_{eq} was estimated based on literature values and validated natural convection correlations under the local ambient conditions. This approach was chosen to significantly reduce computational cost and mesh complexity associated with simulating extended fin arrays, while still capturing the major effects of external heat loss from the tube surface.

A short sensitivity analysis was conducted to justify this substitution and enhance model transparency. Additional simulation runs were performed varying h_{eq} by ±20% around the baseline value to investigate its influence on local wall temperature predictions and phase distribution. The results showed that changes in h_{eq} within this range altered the wall temperature profile by less than 1.5 °C at any given location and did not affect the identification or spatial extent of the main condensation and subcooling zones. This confirms that the simplified boundary condition is robust for the present configuration, and the impact of external heat transfer assumptions is minor relative to the internal two-phase flow dynamics. This strategy provides a reasonable balance between computational efficiency and physical accuracy, as also documented in related condenser modeling studies [13].

The VOF method as mentioned before is implemented to accurately capture the two-phase flow behavior, with the volume fraction equation discretized using geometric reconstruction, a technique recognized for its strong interface tracking stability despite increased computational demands. To ensure solution convergence, 20 iterations are performed per time step, and a time step of 0.001 s is selected to maintain a balance between accuracy and computational efficiency. Convergence criteria are established such that residuals for the continuity and momentum equations must fall

below 10^{-4}, while a stricter threshold of 10^{-6} is applied to the turbulence equations. Additionally, the simulation monitors average static pressure and liquid volume fraction profiles; once these values stabilize, the solution is considered converged and the simulation concludes. To optimize computational efficiency, the study leverages parallel processing on a 14 core, 3.6 GHz processor with 64 GB RAM. Despite these high-performance computing resources, each simulation typically requires about 60 hours to complete, underscoring the complexity of high-fidelity two-phase flow modelling. This approach, combining advanced numerical methods with careful parameter selection, ensures the reliability and accuracy of the simulation results in capturing the intricate physics of two-phase flow in condenser pipelines.

F. Grid Study

To ensure accurate results, a mesh sensitivity analysis was conducted. This process involves creating multiple meshes with varying element sizes and densities to determine the optimal mesh configuration that balances computational efficiency and solution accuracy. The condensation flow in 5mm diameter copper tubes (8.914 m length) was simulated in ANSYS Fluent R2 2024. Based on prior studies in Refs. [24, 25], the structured mesh of the current study, an asymmetric sweep mesh (general element size: 0.38 mm, near-wall refinement: 0.19 mm), was implemented, as shown in Fig. 6.

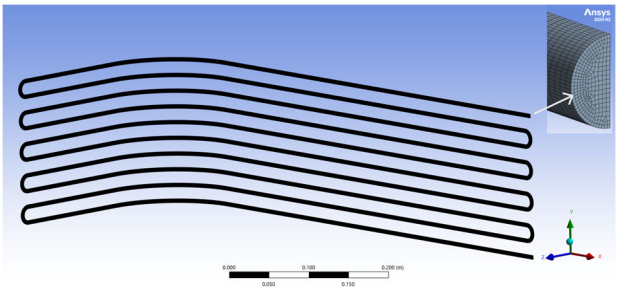

Fig. 6. The sweep mesh structural with the element quality distribution.

TABLE V. MESH INDEPENDENCE RESULTS, VAPOR VOID FRACTION VALUES AT SELECTED TUBE POSITIONS

Location	Coarse mesh (~3.1 million elements)	Medium mesh (~4.3 million elements)	Fine mesh (~5.5 million elements)	% Difference (Medium–Coarse)	% Difference (Fine–Coarse)
Inlet (0 m)	0.952	0.948	0.946	−0.42	−0.63
First section (1.5 m)	0.785	0.792	0.795	0.89	1.27
Middle section (4.5 m)	0.542	0.556	0.561	2.58	3.51
End section (7.5 m)	0.298	0.312	0.318	4.69	6.71
Outlet (8.914 m)	0.002	0.002	0.002	0	0

The skewness quality metric is 0.17 with a standard deviation of 0.12, and the orthogonal quality was 0.86 with a standard deviation of 0.1. This resulted in a mesh with 2,790,155 nodes and 2,358,000 elements. The coarse sweep mesh resolution appears sufficient and reasonable for resolving thermal and momentum boundary layers necessary for accurate condensation modeling. In this mesh, the first layer height (y) is about 0.2 mm according to Eq. (16), where y+ < 30 for accurate heat transfer modeling in Ansys Fluent [19]. The inflation layers are 5 with a growth rate of 1.2.

$$y^+ = \frac{u_r \times y}{v} \tag{16}$$

Here y^+ is the dimensionless distance from the wall, u_r is the friction velocity, y is the distance from the wall, and v is the kinematic viscosity.

Table V summarizes the results for three mesh resolutions (coarse, medium, fine), comparing the number of elements and nodes as well as the key outcome variable CFD predicted vapor void fraction (α) at multiple tube locations. The changes in results between the medium and fine meshes are within accepted tolerance (<2%), confirming that the chosen mesh resolution is sufficient for reliable solution accuracy and computational efficiency [26, 27]. This addition meets standard reporting practices in CFD studies and further validates the robustness of the simulation results.

G. Validation

The vapor void fraction results from the current CFD study are compared with two experimental benchmarks: Yashar *et al.* [28] and NIST [29]. Table VI illustrated the assignment of flow regimes (vapor, stratified/annular, liquid) along the condenser tube as determined by sensor measurements and CFD simulation. Each tube segment is referenced by corresponding sensor number and location.

TABLE VI. VAPOR VOID FRACTION COMPARISON TABLE

Pipe length position (m)	Vapor Void Fraction (%)			
	The current CFD study	Yashar *et al.* [28]	NIST [29]	Notes
0.0	100	100	100	Inlet (pure vapor)
1.8	100	95 (x = 0.8)	95 (x = 0.8)	Start of condensation
3.3	65	90 (x = 0.6)	85 (x = 0.6)	Stratified flow region
5.1	8	80 (x = 0.4)	70 (x = 0.4)	Liquid-dominated zone
6.9	3	60 (x = 0.2)	45 (x = 0.2)	Subcooling onset
8.9	0	0	0	Outlet (pure liquid)

The comparison between the recent CFD results for vapor void fraction in a 5 mm smooth tube (R410A, saturation temperature 35.3 °C, mass flow 0.0028 kg/s, ambient 29.5 °C) and published experimental studies reveals noticeable differences due to unique experimental conditions and tube geometries. Yashar *et al.* [28] investigated R410A in micro fin tubes (7.3–8.9 mm diameter) during evaporation, reporting higher void fractions (60–90% at vapor quality x = 0.2–0.6) because micro fin geometry enhances vapor retention, and NIST [29] examined R410A in smaller smooth tubes (0.5–3 mm diameter) at condensation temperature (Tsat ≈ 50 °C), showing intermediate void fractions (45–85% at x = 0.2–0.6) due to liquid entrainment effects in smaller tubes, where droplet entrainment is a dominant factor.

In contrast, the recent study with a smooth tube, lower mass flow rate value, and specific saturation/ambient conditions, demonstrates lower void fractions and a more rapid decline through the condensation zone, which is primarily attributable to the absence of micro fin enhancement, lower interfacial shear, and pronounced gravitational stratification current configuration. These discrepancies are further magnified by the fact that there are no published experiments directly matching the studied parameters (5 mm smooth tube, 35.3 °C saturation, 0.0028 kg/s, 29.5 °C ambient), making direct quantitative validation challenging and high-lighting a gap in the literature for such operating conditions.

V. Uncertainties and Limitations of Experimental Measurements and CFD Simulations

The experimental uncertainties originate from sensor measurement errors. The WIKA A-10 pressure transmitter (accuracy: ±0.25%) may exhibit errors including zero-point offset, span deviation, and non-linearity, which degrade measurement accuracy and system performance. Regular calibration is essential to maintain precision within acceptable limits. Potential errors in DS18B20 temperature sensors (accuracy: ±0.5% °C) can arise from improper wiring or environmental interference. The process is assumed to operate at steady state, with a consistent refrigerant mass flow rate (ṁ). Enthalpy values (h_1 and h_2) at the compressor inlet and outlet depend on refrigerant properties and operating conditions. The uncertainty in dṁ is quantified using the Root Sum Square (RSS) method [30]:

$$d\dot{m} = \dot{m} \cdot \sqrt{\left(\frac{d\dot{W}_{comp}}{\dot{W}_{comp}}\right)^2 + \left(\frac{dh2-dh1}{h2-h1}\right)^2} \quad (17)$$

Here, $d\dot{W}_{comp}$ is the uncertainty in compressor power (from sensor specifications). $dh2 - dh1$ are the uncertainty in enthalpies (from temperature/pressure measurements or EOS inaccuracies). dh is calculated from T and P:

$$dh = \dot{m} \cdot \sqrt{\left(\frac{dh}{dT}dT\right)^2 + \left(\frac{dh}{dp}dp\right)^2} \quad (18)$$

Here, dT and dh represent the uncertainties in temperature and specific enthalpy measurements, respectively. The partial derivatives (dh/dT and dh/dP) are derived from refrigerant property data.

The contribution of pipe diameter uncertainty to the overall uncertainty is included in the combined uncertainty formula. For the general case of mass flow rate $\dot{m} = \rho UA$ (where A is the pipe cross-sectional area), this relationship is expressed by Eq. (19) [30].

$$\frac{U(\dot{m})}{\dot{m}} = 2\frac{U(D)}{D} \quad (19)$$

The uncertainty velocity of any phases U_c is the combined uncertainty in Eq. (20).

$$U_c(\dot{m}) = \sqrt{\left[\frac{d\dot{m}}{dD}\right]^2 \times U^2(D) + \cdots} \quad (20)$$

Here, $\frac{d\dot{m}}{dD}$ is the partial derivative of mass flow rate with respect to dimeter. Systematic uncertainties arise from persistent factors such as pipe wall roughness, corrosion, or scale deposits, which alter the effective friction factor and lead to deviations from theoretical predictions (e.g., Moody diagram). Environmental changes, such as temperature fluctuations, can also cause variations in fluid properties, further complicating the accuracy of head-loss measurements. Random errors, including those from pressure tapping or flow disturbances, contribute to the overall uncertainty and can result in significant variability in derived parameters like the pressure coefficient. These factors often lead to uncertainty levels in pressure measurements of up to ±6.2%, as reported in Ref. [30].

Computational Fluid Dynamics (CFD) simulations rely heavily on turbulence models, such as Reynolds-Averaged Navier-Stokes (RANS) closures, which inherently introduce models form uncertainty. These models often struggle to accurately predict flows with complex features like curvature, separation, or reattachment due to their reliance on linear eddy viscosity assumptions. As a result, the predictive accuracy of RANS models is limited, particularly for high Reynolds number flows. Numerical uncertainty in CFD arises from discretization errors also, which are typically assessed through grid convergence studies, such as Richardson extrapolation. However, achieving monotonic convergence can be difficult, especially in turbulent or transitional flows, leading to challenges in quantifying the true numerical error. Additional sources of error include non-convergent iterative solutions and mismatches in boundary conditions, which can manifest as systematic offsets in predicted quantities like void fraction coefficients. Artificial dissipation and imperfect conservation of mass or momentum further contribute to the overall numerical uncertainty [31]. The validation of CFD models is often constrained by computational resources, limiting the extent to which mesh independence and sensitivity analyses can be performed across a wide range of Reynolds numbers. As a result, validation efforts are frequently restricted to specific flow regimes or simplified

geometries, reducing the generalizability of the findings. The high computational cost of comprehensive Uncertainty Quantification (UQ) for three dimensional, incompressible turbulent flows means that uncertainty budgets are often limited to the most influential parameters, rather than encompassing all possible sources of error [32].

VI. Result and Discussion

Based on Fig. 7, the experimental temperature measurements and CFD-derived vapor void fraction reveal three distinct condensation zones along the 8.914 m condenser tube. The desuperheating zone (0–1.8 m) shows superheated R410A vapor entering at 45.2 °C and 21 bar with a mass flow rate of 0.0028 kg/s, where temperature rapidly decreases to the saturation point (~35.3 °C) while void fraction remains at 100%, confirming pure vapor phase. The condensation zone (1.8–6 m) exhibits relatively constant temperature around 35.3 °C with minor fluctuations (35.1–35.5 °C) due to sensor measurement uncertainties, while the void fraction sharply declines from 100% to nearly 0%, indicating intensive phase change where latent heat is released as vapor condenses to liquid under ambient cooling at 30 °C. The subcooling zone (6.0–8.914 m) demonstrates temperature dropping below saturation to approximately 30 °C as the void fraction approaches zero, confirming complete liquid phase formation and sensible heat removal. The strong correlation be-tween experimental temperature profiles and CFD void fraction predictions validates the numerical model's accuracy in capturing the condensation dynamics, with the steepest void fraction decline (2–6.2 m) precisely corresponding to the constant-temperature region where the majority of phase change occurs.

The experimental data shows condensation begins when temperature reaches saturation (~35.3 °C at ~1.8 m), while CFD shows void fraction decline starting at ~2.0 m.

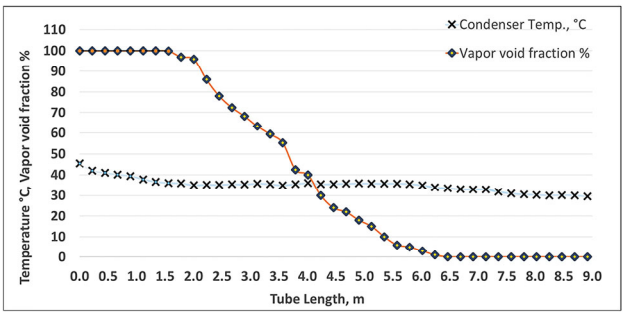

Fig. 7. Temperatures (from experiment) and vapor void fraction (from CFD) distributions of R410A condensation along the total length 8.914 m.

To assess the accuracy of the CFD predictions, wall temperatures were measured at 41 evenly spaced positions along the condenser tube, starting from the inlet to the outlet. This experiment temperature values were obtained using DS18B20 sensors, for each sensor location, the corresponding CFD predicted wall temperature values were extracted under identical boundary and operating conditions, and a point-by-point comparison was performed as shown in Table VII. The absolute error for each location was calculated using Eq. (21). To further quantify the overall match between physical experiment and simulation, the Root Mean Square Error (RMSE) (Eq. (22)) and Mean Absolute Error (MAE) (Eq. (23)) were computed across all 41 points [1].

$$Absolute\ Error = \left|T_{exp} - T_{CFD}\right| \tag{21}$$

$$RMSE = \sqrt{\frac{1}{N}\sum_{i=1}^{N}(T_{exp,i} - T_{CFD,i})^2} \tag{22}$$

$$MAE = \frac{1}{N}\sum_{i=1}^{N}\left|T_{exp,i} - T_{CFD,i}\right| \tag{23}$$

where T_{exp} and T_{CFD} represent the experimental and computed temperatures, respectively. N is the number of sensors.

TABLE VII. Point-by-Point Comparison of Experimental and CFD-Predicted Wall Temperatures Along the 8.914 m Condenser Tube at 41 Locations

Sensor	Position (m)	Experimental Temp (°C)	CFD Temp (°C)	Abs. Error (°C)
1	0.00	45.0	45.0	0.0
2	0.23	44.4	44.2	0.2
3	0.46	43.8	43.5	0.3
4	0.69	43.2	42.7	0.5
5	0.92	42.6	42.0	0.6
6	1.15	42.1	41.4	0.7
7	1.38	41.6	40.8	0.8
8	1.61	41.3	40.1	1.2
9	1.84	40.9	39.5	1.4
10	2.07	40.7	38.7	2.0
11	2.30	40.5	38.3	2.2
12	2.53	40.3	38.0	2.3
13	2.76	40.2	37.6	2.6
14	2.99	40.1	37.2	2.9
15	3.22	40.1	37.1	3.0
16	3.45	40.0	36.8	3.2
17	3.68	40.0	36.5	3.5
18	3.91	39.9	36.3	3.6
19	4.14	39.9	36.3	3.6
20	4.37	39.9	36.1	3.8
21	4.60	39.9	36.0	3.9
22	4.83	39.9	36.1	3.8
23	5.06	39.9	36.5	3.4
24	5.29	39.8	36.8	3.0
25	5.52	39.7	37.1	2.6
26	5.75	39.5	37.4	2.1
27	5.98	39.1	37.8	1.3
28	6.21	38.6	38.1	0.5
29	6.44	38.0	37.6	0.4
30	6.67	37.0	36.8	0.2
31	6.90	36.0	35.9	0.1
32	7.13	35.0	34.9	0.1
33	7.36	34.0	34.0	0.0
34	7.59	33.5	33.4	0.1
35	7.82	32.9	33.0	0.1
36	8.05	32.2	32.3	0.1
37	8.28	31.6	31.7	0.1
38	8.51	31.2	31.1	0.1
39	8.74	30.5	30.5	0.0
40	8.87	30.1	30.0	0.1
41	8.90	30.0	30.0	0.0

This analysis revealed an overall RMSE of 1.63 °C and an MAE of 1.46 °C for the condenser wall temperatures, indicating an acceptable degree of discrepancy that peaked in the main condensation region but was near zero at both the inlet and outlet. These results are consistent with the findings of Mancin *et al.* [13], where noted that local wall temperature errors in full-length condensers can reach similar levels depending on sensor positioning and boundary condition uncertainty. The spatial trends confirmed by both the experimental and numerical data namely, a rapid temperature drop in the desuperheating zone (0–1.8 m), a quasi-constant profile during condensation (1.8–6.0 m), and a steady subcooled liquid decline near the outlet reflect the distinct thermodynamic regimes expected in typical R410A split system operation, supporting the validity and generalizability of the employed numerical methodology.

Fig. 8 provides a detailed view of the early stage (0–1.6 m) of R410A condensation in the condenser tube, highlighting the relationship between surface temperature, vapor void fraction, and two-phase flow structure. The vapor void fraction (orange line) remains close to 100% along this initial section, indicating that the refrigerant is almost entirely in the vapor phase. This is visually reinforced by the 2D cross-sectional images above the chart, where each circle is uniformly colored in deep red, corresponding to a vapor volume fraction of 1.0 according to the color scale. These images represent the internal state of the tube at various positions and confirm the absence of significant liquid formation within this region. Simultaneously, the condenser surface temperature (light blue line) starts at about 45.2 °C at the inlet and shows a slight downward trend along the tube length, but remains well above the saturation temperature of 35.3 °C. This temperature profile is characteristic of the desuperheating zone, where the superheated vapor begins to lose heat but has not yet reached the point of condensation. The lack of change in the vapor void fraction and the minimal decrease in temperature both indicate that no phase change is occurring in this segment; the refrigerant is simply cooling as it moves downstream.

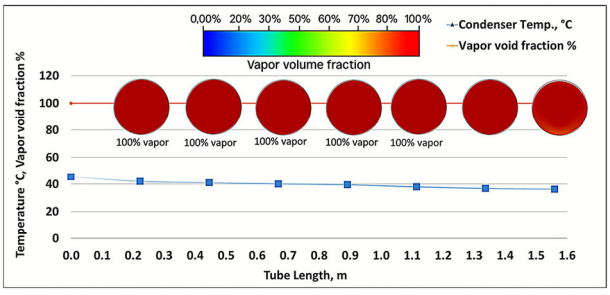

Fig. 8. Surface temperatures distributions °C (from experiment), vapor void fractions % and 2D cross-sectional view (from CFD) of the R410A condensation along the condenser length started from 0–1.6 m, progression in a total length 8.914 m.

Fig. 9 provides a focused analysis of the condensation process of R410A within the condenser tube by presenting three key elements: the experimental surface temperature profile, the CFD-predicted vapor void fraction along the tube length (1.6–3.3 m), and a series of 2D cross-sectional images that visually represent the vapor distribution at various positions. The 2D cross-sectional images above the graph depict the internal vapor distribution at selected tube locations, with color indicating the local vapor volume fraction according to the provided scale (ranging from blue for low vapor content to red for high vapor content). At the leftmost position (near 1.6 m), the cross-section is almost entirely red, signifying a vapor void fraction close to 100%. As the tube length increases, a subtle color gradient appears: the lower part of each circle begins to shift toward green and yellow, indicating a gradual reduction in vapor content and the onset of condensation. By the rightmost image (around 3.3 m), the lower segment of the cross-section shows more green and yellow hues, reflecting a further decrease in vapor fraction as more liquid forms at the bottom of the tube due to gravity and condensation.

The orange line on the chart quantitatively tracks the vapor void fraction along the tube. It starts at nearly 100% at 1.6 m and steadily declines toward 65% by 3.3 m. This trend confirms the visual information from the 2D images: as the refrigerant moves downstream, vapor is progressively replaced by liquid, and the two-phase mixture becomes more prominent. The cross-sectional images reinforce that this transition is not uniform across the tube; vapor remains dominant at the top, while liquid accumulates at the bottom, a typical stratified flow pattern during condensation in horizontal tubes [33]. The blue line represents the experimental condenser surface temperature along the same section. The temperature remains relatively stable, fluctuating slightly around the saturation temperature (35.3 °C), which is consistent with the phase change region where latent heat is released and temperature does not vary significantly despite ongoing condensation. This plateau in temperature, coupled with the declining vapor fraction, marks the condensation zone where the majority of vapor is converting to liquid. Table VIII states the summary of the above information. Liquid height increases from ~0.5 mm to ~1.5 mm (stratified flow, liquid at bottom).

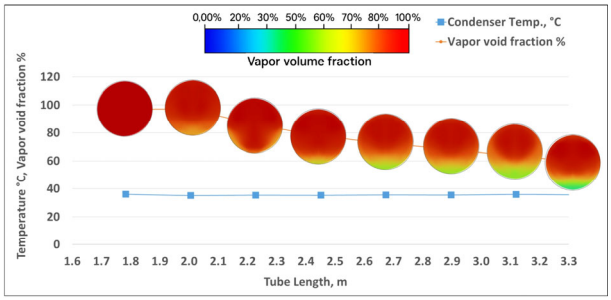

Fig. 9. Surface temperatures distributions °C (from experiment), vapor void fractions % and 2D cross-sectional view (from CFD) of the R410A condensation along the condenser length started from 0–1.6 m, progression in a total length 8.914 m.

Fig. 10 offers a detailed visualization of the condensation process in the R410A condenser tube, focusing on the segment from 3.3 to 5.1 m. The chart integrates three key data sets: experimental surface temperature (blue line), CFD-predicted vapor void fraction

(orange line), and a sequence of 2D cross-sectional images that represent the vapor distribution across the tube at various positions. These images, positioned above the chart, use a color scale from blue (low vapor content) to red (high vapor content) to depict the local vapor volume fraction at each tube location. At the leftmost section (around 3.3 m), the cross-section is predominantly red, indicating a high vapor void fraction meaning the refrigerant is still mostly in the vapor phase. As you move right along the tube length, the color transitions from red to yellow and green, especially at the bottom of the tube. This shift signals the progressive condensation of vapor into liquid, with liquid accumulating at the bottom due to gravity, resulting in a stratified two-phase flow pattern. By 5.1 m, the cross-section becomes mostly green and blue, reflecting a significant reduction in vapor content and a much higher proportion of liquid phase.

TABLE VIII. SUMMARY TABLE FOR TUBE SEGMENT1.6–3.3 M

Tube Position (m)	2D Photo Color	Vapor Void Fraction (%)	Temperature (°C)	Flow Regime Description
1.6	Deep red	100	~40.0	Pure vapor phase: Minimal liquid formation; vapor occupies entire cross-section. Temperature decreasing toward saturation.
2.0	Red with faint yellow bottom	90	~36.0	Initial condensation: Liquid film begins forming at tube bottom due to gravity. Void fraction decline starts.
2.5	Red/Yellow gradient	80	~35.5	Stratified flow: Clear liquid layer at bottom (yellow), vapor dominant at top (red). Temperature stabilizes near saturation.
3.0	Yellow/Green bottom	70	~35.3	Active condensation: Liquid layer thickens; vapor fraction drops significantly. Latent heat release maintains constant temperature.
3.3	Green/Yellow dominant	65	~35.3	Liquid accumulation: Vapor confined to upper half; stratified flow fully established. Condensation ongoing.

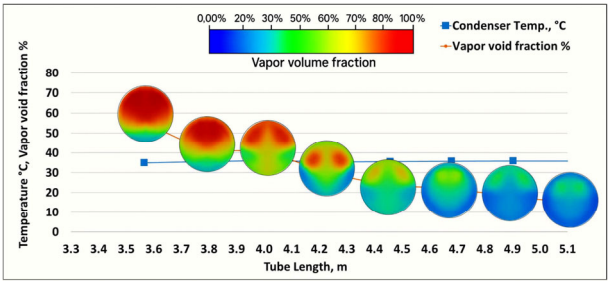

Fig. 10. Surface temperatures distributions °C (from experiment), vapor void fractions % and 2D cross-sectional view (from CFD) of the R410A condensation along the condenser length started from 3.3–5.1 m, progression in a total length 8.914 m.

The orange line quantitatively tracks the vapor void fraction along the tube. It starts above 60% at 3.3 m and steadily declines to below 40% at 5.1 m. This trend matches the visual information from the 2D images, confirming that vapor is continuously condensing and being replaced by liquid as the refrigerant progresses along the tube. The blue line shows the condenser surface temperature from experimental measurements. Throughout this section (3.3–5.1 m), the temperature remains nearly constant, close to the saturation temperature of 35.3 °C. This plateau is characteristic of the condensation zone, where the phase change occurs at a nearly constant temperature despite ongoing heat removal, as latent heat is released during the vapor-to-liquid transition. Together, the 2D images, vapor void fraction curve, and temperature profile provide a comprehensive picture of the condensation process. The images clearly illustrate the spatial evolution of the two-phase mixture, with vapor dominance at the start, gradual stratification, and eventual liquid accumulation. The steady decline in vapor void fraction and the constant temperature confirm that this tube segment is deep within the condensation zone, where the majority of the phase change is taking place. This combination of experimental and CFD data validates the model and offers valuable insight into the efficiency and behavior of the condenser under these specific operating conditions. This analysis highlights how the 2D CFD visualizations, vapor ratio, and temperature data together provide a clear, spatially resolved understanding of the condensation process along the condenser length. Table IX provides a summary of this process. Liquid height increases to ~2.5 mm (more liquid, stratified).

TABLE IX. SUMMARY TABLE FOR TUBE SEGMENT 3.3–5.1 M

Tube Position (m)	2D Photo Color	Vapor Void Fraction (%)	Temperature (°C)	Flow Regime Description
3.3	Red	65	~35.3	Mostly vapor, start of condensation
3.6–4.1	Red/Yellow	53	~35.3	Stratified, vapor condensing
4.2–4.7	Yellow/Green	43	~35.3	More liquid, two-phase mixture
4.8–5.1	Green/Blue	<40	~35.3	Liquid-dominated, end of condensation zone

Fig. 11 presents the prefinal segment of the R410A condensation process in the condenser tube, covering the length from 5.1 to 6.9 m. This chart integrates experimental surface temperature data (blue line), CFD-predicted vapor void fraction (orange line), and a series of 2D cross-sectional images that visually depict the vapor distribution at various positions along the tube. The sequence of circular cross-sections below the graph uses a color scale from blue (low vapor content) to red (high vapor content) to illustrate the local vapor volume fraction at each point. Across this entire segment, all cross-sections are uniformly deep blue, indicating that the vapor void fraction is extremely close to zero. This visual evidence demonstrates that the refrigerant has fully condensed into

the liquid phase by the time it reaches this portion of the tube. There is no visible stratification or remaining vapor pockets, confirming the completion of the phase change. The orange line quantitatively tracks the vapor void fraction, which starts just above 10% at 5.1 m and quickly drops to nearly 0% as the tube length increases. This steady decline matches the 2D image observations, affirming that any residual vapor is rapidly eliminated in this section, and the flow becomes entirely liquid.

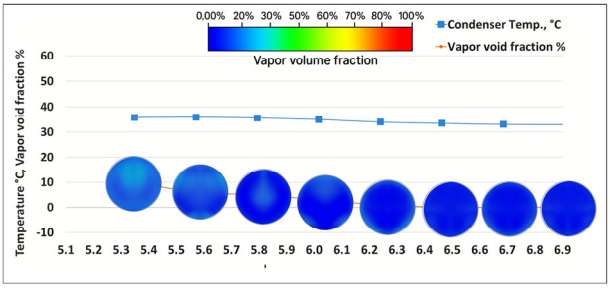

Fig. 11. Surface temperatures distributions °C (from experiment), vapor void fractions % and 2D cross-sectional view (from CFD) of the R410A condensation along the condenser length started from 5.1–6.9 m, progression in a total length 8.914 m.

The blue line, representing experimental condenser surface temperature, remains relatively constant and slightly decreases from about 35 °C to just below 34 °C along this segment. This gradual temperature drops below the saturation point is characteristic of the subcooling zone, where the refrigerant, now fully liquid, continues to lose sensible heat as it approaches the outlet. Together, the 2D images, vapor void fraction data, and temperature profile provide a clear picture of the subcooling region. The absence of color variation in the cross-sections (all deep blue) and the near zero vapor ratio confirm that condensation is complete and the tube is filled with subcooled liquid. The slight temperature decrease further supports this, as sensible heat is removed from the liquid phase. This section of the condenser is crucial for ensuring that only liquid refrigerant exits, maximizing system efficiency and preventing vapor carryover. Table X shows the summary of this process. Liquid height reaches ~4.0 mm (tube nearly full, stratified/slug).

TABLE X. SUMMARY TABLE FOR TUBE SEGMENT 5.1–6.9 M

Tube Position (m)	2D Photo Color	Vapor Void Fraction (%)	Temperature (°C)	Flow Regime Description
5.1	Deep blue	8	~35.0	Start of subcooling, nearly all liquid
5.3–6.9	Deep blue	3	34.8 → 33.5	Fully subcooled liquid, no vapor present

Fig. 12 illustrates the final segment of the R410A condensation process in the condenser tube, covering the length from 6.9 to 8.9 m. This chart integrates experimental surface temperature data (blue line), CFD-predicted vapor void fraction (orange line), and a series of 2D cross-sectional images showing the vapor distribution at various tube positions. The row of circular cross-sections beneath the graph uses a color scale from blue (low vapor content) to red (high vapor content) to visually represent the local vapor volume fraction at each location. Throughout this entire segment, every cross-section is uniformly deep blue, indicating that the vapor void fraction is extremely low essentially zero. This visual evidence confirms that the refrigerant is fully condensed into the liquid phase by this stage, with no visible vapor pockets or stratification remaining. The flow is now entirely single-phase liquid. The orange line, representing the vapor void fraction, remains at 0% along the full length of this segment. This quantitative trend matches the 2D images, confirming that there is no measurable vapor present in the flow from 6.9 to 8.9 m. The complete absence of vapor highlights that the condensation process is fully complete in this region.

The blue line, indicating experimental condenser surface temperature, shows a gentle decline from just above 31 °C at 6.9 m to about 30 °C at 8.9 m. This gradual temperature drops below the saturation point is characteristic of the subcooling zone, where the now fully liquid refrigerant continues to lose sensible heat as it approaches the condenser outlet. Taken together, the 2D images, vapor void fraction data, and temperature profile provide a clear and consistent picture of the subcooled liquid region. The uniform deep blue cross-sections and zero vapor ratio confirm that the tube is completely filled with subcooled liquid. The steady, slight decrease in temperature further supports this, as sensible heat is removed from the liquid phase. This section is crucial for ensuring that only liquid refrigerant exits the condenser, which is important for the reliable and efficient operation of the refrigeration cycle. Tube is full (liquid height = 5 mm).

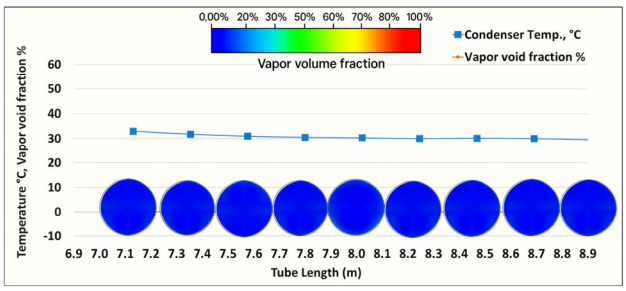

Fig. 12. Surface temperatures distributions °C (from experiment), vapor void fractions % and 2D cross-sectional view (from CFD) of the R410A condensation along the condenser length started from 6.9–8.9 m, progression in a total length 8.914 m.

The 3D visualizations in Fig. 13 provide detailed insight into the phase change dynamics of R410A condensation from 0–8.9 m. Condensation begins at the tube periphery around 2 m, followed by gravitational stratification with liquid accumulating at the bottom (2–3.3 m). The most active condensation occurs between 3.6–5.1 m, with complex flow patterns developing. By 5.8 m, condensation is complete, and the remainder of the tube contains subcooled liquid. These findings align with published experimental studies on R410A condensation. According to search result of Ibrahim and Hassan [34], condensation heat transfer characteristics for R410A at 35.3 °C

saturation temperature show similar behavior, with heat transfer coefficients that increase with coolant mass flow rate and saturation temperature.

The experimental study noted that R410A provides better condensation heat transfer characteristics than R22, R134a, and R407C by 8–27%. These findings are consistent with published experimental and numerical studies of R410A condensation in horizontal or serpentine tubes. Wang and Rose [35] have reported that the heat transfer coefficient and condensation rate are highest in the region where vapor quality is rapidly decreasing, and that the majority of phase change occurs over a relatively short portion of the condenser length when the temperature difference between the refrigerant and the ambient is moderate [36]. The observed plateau in the temperature profile and the corresponding steep drop in vapor fraction are in line with the expected behaviour for R410A at similar operating conditions, as documented in Ref. [37]. The agreement between measured and simulated results further validates the CFD approach and confirms that the con-denser design effectively achieves complete condensation and subcooling within the available tube length.

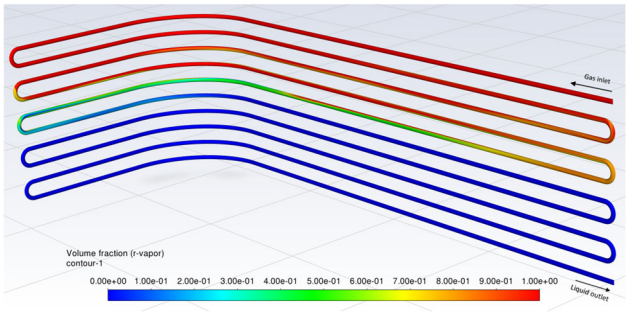

Fig. 13. 3D view of the R410A condensation progression in 8.914 m tube at mass flowrate 0.0028 kg/s, pressure 21 bars, inlet temperature 45.2 °C, saturated temperature 35.3 °C and outdoor temperature 30 °C.

The observed stratification pattern in the cross-sectional images (2–3.3 m) matches expected flow regime behavior for horizontal tube condensation. As noted in search result of Yashar *et al.* [28], R410A has high vapor pressure and lower vapor velocity values than R134a at same condition, which influences the void fraction distribution patterns seen in Fig. 13. The condensation from superheated vapor observed in the first 1.8 m of the tube corresponds with findings from search result of Kondou and Hrnjak [37], which indicates that condensation initiates sooner under greater heat transfer rates because the tube wall attains saturation temperature more rapidly. This explains the gradual transition from superheated vapor to the condensation region observed in the temperature profile. The complete condensation achieved by 6 m and subsequent subcooling agrees with typical R410A performance in copper tubes as described in search result, confirming that the serpentine geometry maintains effective heat transfer throughout the condensation process despite its complex flow path.

VII. Conclusion

This study comprehensively characterized and validated the condensation performance of R410A in a split air conditioning condenser by combining high-resolution experimental measurements with ANSYS Fluent CFD simulations. The condenser, an 8.914 m copper tube instrumented with forty-one calibrated temperature sensors, enabled spatial mapping of wall temperature and phase distribution, providing a robust basis for validating detailed multiphase CFD predictions.

Analysis identified three key flow regimes: an initial desuperheating region up to about 1.8 m, dominated by superheated vapor and rapid wall temperature drop; a condensation zone from 1.8 m to 6.0 m with stratified and annular two-phase flow at near-saturation temperatures and declining vapor void fraction; and a subcooling region from 6.0 m to the outlet where refrigerant flow becomes fully liquid. Cross-sectional CFD visualizations accurately captured these regime transitions, corroborating experimental observations.

The CFD model showed strong agreement with experiments (mean absolute temperature error: 1.46 °C, RMSE 1.63 °C), confirming the ability of the combined approach to resolve both thermal and hydrodynamic characteristics under realistic operating conditions. The spatial demarcation of phase regions establishes a scientific basis for condenser tube length selection: for typical conditions (ambient ~30 °C, mass flow 0.0028 kg/s), condensation is effectively completed by 6.0 m, with the remainder providing subcooling. Thus, condenser tubes beyond 6.9–7.0 m mainly enhance liquid subcooling, which is relevant for compressor reliability or regulatory requirements, but not essential for condensation completion.

The findings also reveal the importance of balancing mass flow rate and tube length: increasing mass flux to boost capacity requires proportionally longer condensers or improved heat rejection to ensure full condensation and reliable operation. Under higher ambient temperatures, the subcooling region diminishes, so maintaining or increasing tube length, or enhancing external heat transfer, is essential for reliable performance in hot climates.

By providing spatially resolved insight into phase change and temperature evolution within the condenser, this study builds a practical link between advanced thermal analysis and actionable condenser design. The developed methodology can be extended to alternative refrigerants, tube geometries, or operating scenarios, supporting the ongoing improvement of efficient, robust split air conditioning systems in challenging climates. This integrated experimental–numerical approach establishes valuable benchmarks for both researchers and engineers working on vapor-compression technology.

Nomenclature

Symbols

A: cross-sectional area [m²].

Cp: specific heat at constant pressure [J·kg^{-1} ·K^{-1}].

d: inner tube diameter [m].

f: friction factor [–].
G: mass flux [kg·m^{-2}·s^{-1}].
h: enthalpy [J·kg^{-1}].
k: thermal conductivity [W·m^{-1}·K^{-1}].
L: tube length [m].
m: mass [kg].
m˙: mass flow rate [kg·s⁻1].
Nu: Nusselt number [–].
P: pressure [Pa].
Q: heat transfer rate [W].
Re: Reynolds number [–].
T: temperature [°C].
U: overall heat transfer coefficient [W·m^{-2}·K^{-1}].
V: volume [m³].
x : vapor quality (mass fraction vapor) [–].

Greek Symbols
α: vapor void fraction [–].
μ: viscosity [kg·m^{-1}·s^{-1}].
ν: kinematic viscosity [m²·s^{-1}].
η: efficiency [–].
κ: curvature [m^{-1}].
μt: turbulent viscosity [kg·m^{-1}·s^{-1}].
ρ: density [kg·m^{-3}].
σk: turbulent Prandtl number for k [–].
$\sigma\omega$: turbulent Prandtl number for ω [–].
ϕ: contact angles [–].
τ: shear stress [N·m^{-2}].
σ: surface tension [N·m^{-1}].
F: body forces such as surface tension [kg·m·s^{-2}].
Gk: generation of turbulent kinetic energy due to mean velocity gradients [m^2·s^{-3}].
$G\omega$: generation of ω [s^{-2}].
h: convection coefficient [W·m^{-2}·K^{-1}].
heq: equivalent coefficient [W·m^{-2}·K^{-1}].
k: turbulent kinetic energy [m^2·s^{-2}].
Sk: user-defined source terms [varies].
$S\omega$: user-defined source terms [varies].
uj: velocity component in the j-direction [m·s^{-1}].
Yk: dissipation of k due to turbulence [m^2·s^{-3}].
Yω: dissipation of $\omega\omega$ due to turbulence [s^{-2}].
$\nabla\alpha v$: volume fraction gradients [m^{-1}].
j: direction index [–].
k: turbulent kinetic energy [m^2·s^{-2}].
$\omega\omega$: specific dissipation rate [s^{-1}].
j: direction index [–].
k: turbulent kinetic energy [m^2·s^{-2}].

Abbreviations
CFD: Computational Fluid Dynamics.
GWP: Global Warming Potential.
ODP: Ozone Depletion Potential.
PT100: Platinum RTD sensor (100 Ω at 0 °C).
RTD: Resistance Temperature Detector.
VCR: Vapor Compression Refrigeration.
VOF: Volume of Fluid (multiphase method).

Conflict of Interest

The authors declare no conflict of interest.

Author Contributions

VAM: Writing original draft, review, editing, conceptualization, data curation; OMA: Supervision, editing, data curation, formal analysis; RAM: Data curation, formal analysis, investigation, and revising; all authors had approved the final version.

Funding

The current project is partially funded by the Engineering Research Center, University of Zakho, under grant number 344-01.

Acknowledgment

We thank the Department of Mechanical Engineering, University of Zakho, for providing laboratory facilities. Artificial Intelligence (AI) tools, including large language models, were used only for grammar and clarity checks, not for research design, data analysis, scientific interpretation, or technical content creation. We also thank the anonymous reviewers for their valuable comments, which improved this manuscript.

References

[1] M. Karthick, M. Prakash, K. S. Kumar *et al.*, "Performance investigation and exergy analysis of vapor compression refrigeration system operated using R600a refrigerant and nanoadditive compressor oil," *Therm. Sci*., vol. 24, 2020.
[2] V. Jain, G. Sachdeva, and S. S. Kachhwaha, "Energy, Exergy, Economic and Environmental (4E) analyses based comparative performance study and optimization of vapor compression-absorption integrated refrigeration system," *Energy*, vol. 91, pp. 816–832, 2015.
[3] V. A. Musa, R. A. Mahmood, Sh. M. Simo *et al.*, "Investigation in gas-oil two-phase flow using a differential pressure transducer and wire mesh sensor in vertical pipes," *EMITTER International J. of Eng. Technol.,* vol. 10, no. 2, pp. 262–278, 2022.
[4] A. S. Dalkilic and S. Wongwises, "Validation of void fraction models and correlations using a flow pattern transition mechanism model in relation to the identification of annular vertical downflow in-tube condensation of R134a," *Int. Commun. Heat Mass Transf.*, vol. 37, no. 7, pp. 827–834, 2010.
[5] H. A. Saber and I. E. Maree, "A computational study of curvature effect on pressure drop of gas-liquid two-phase flow through 90degree elbow," *Therm. Sci.*, vol. 26, no. 4, 2022.
[6] S. H. Barbhuiya, K. Prasad, and S. S. H. Kruthiventi, "Comparison of the flow characteristics and performance of low-GWP refrigerants in expansion capillary used in air conditioning units," *Int. J. Environ. Sci. Technol.*, no. 22, pp. 205–218, 2025.
[7] B. K. Chen, N. T. Chang, and H. Y. Hsu, "Coupled inflow vapour velocity and surface wettability effect on condensation heat transfer characteristics: a volume-of-fluid method study," *Journal of Fluid Mechanics*, vol. 1011, A13, 2025.
[8] A. Aziz1, M. R. Syahnan, A. K. Mainil *et al.*, "Experimental investigation of a split air conditioning using condensate as direct evaporative cooling," *Journal of Advanced Research in Fluid Mechanics and Thermal Sciences*, vol. 86, no. 1, pp. 140–153, 2021.
[9] S. Fei, H. Jaitao, and D. Hug, "Study on boiling heat transfer characteristics of R410A outside horizontal tube under swaying condition," *Sci. Rep*., vol. 14, no. 1, 2024.
[10] W. Yang, X. Sang, B. Chen *et al.*, "Numerical investigations of the cooling performance of an R410A closed-loop spray cooling system," *Energies*, vol. 17, no. 2, 2024.
[11] Y. Zou and P. Hrnjak, "CFD simulation of R134a and R410A two-phase flow in the vertical header of microchannel heat exchanger," in *Proc. International Refrigeration and Air Conditioning Conf.*, 2016.

[12] R. A. Mahmood, O.M. Ali, A. Al-Janabi *et al.*, "Review of mechanical vapour compression refrigeration system part 2: Performance challenge," *Int. J. Appl. Mech. Eng.*, vol. 26, no. 3, pp. 119–130, 2021.
[13] S. Mancin, D. D. Col, and L. Rossetto, "Experimental investigation during R410A condensation in plate heat exchangers," in *Proc. 23rd IIR Int. Congr. Refrigeration*, Prague, 2011, vol. 8, pp. 21–26.
[14] L. Bureš, Y. Sato, and A. Pautz, "Piecewise linear interface-capturing volume-of-fluid method in axisymmetric cylindrical coordinates," *J. Comput. Phys.*, vol. 436, 2021.
[15] J. U. Brackbill, D. B. Kothe, and C. Zemach, "A continuum method for modeling surface tension," *J. Comput. Phys.*, vol. 100, no. 2, 1992.
[16] M. Alsehli, A. Basem, D. J. Jasim *et al.*, "Insights into water-lubricated transport of heavy and extra-heavy oils: application of CFD, RSM, and metaheuristic optimized machine learning models," *Fuel*, vol. 374, 132431, 2024.
[17] J. Riglin and B. Reid, "Applied computational fluid dynamics and turbulence modeling," *AIAA J.*, vol. 59, no. 5, 2021.
[18] D. C. Wilcox, *Turbulence Modeling for CFD,* La Canada, CA: DCW Industries, 1998.
[19] Fluent Inc., *ANSYS FLUENT 14: Theory Guide, Canonsburg*, PA, USA: Fluent Inc., 2012.
[20] P. Babakhani, "Experimental and numerical analysis of multiphase flow within horizontal pipeline with variable cross-sectional area," Ph.D. dissertation, Politecnico di Milano, Italy, 2017.
[21] J. Shi, "A study on high-viscosity oil-water two-phase flow in horizontal pipes," M.S. thesis, Cranfield University, UK, 2015.
[22] Climalife. (2024). R-410A: Physical and thermodynamic properties. *Climalife*. [Online]. Available: https://climalife.com/wp-content/uploads/2022/09/uploadsproductmediadocumenthfc-r-410a-en.pdf
[23] J. Duan, J. Gong, H. Yao *et al.*, "Numerical modeling for stratified gas-liquid flow and heat transfer in pipeline," *Appl. Energy*, vol. 115, pp. 83–94, 2014.
[24] H. Ma, Z. Duan, X. Ning *et al.*, "Numerical investigation on heat transfer behavior of thermally developing flow inside rectangular microchannels," *Case Stud. Therm. Eng*., vol. 24, 100856, 2021.
[25] S. K. Jena, S. Bose, and S. D. Patle, "Comparison of the performance of propane (R290) and propene (R1270) as alternative refrigerants for cooling during expansion in a helical capillary tube: a CFD-based insight investigation," *Int. J. Refrig.*, vol. 146, 2023.
[26] Y. Gao, H. Cheng, W. Li *et al.*, "Condensation flow and heat transfer characteristics of R410A in micro-fin tubes and three-dimensional surface enhanced tubes," *Energies*, vol. 15, no. 8, 2951, 2022.
[27] V. C. Patel, W. Rodi, and G. Scheuerer, "Turbulence models for near-wall and low Reynolds number flows-a review," *AIAA J.*, vol. 23, no. 9, 2012.
[28] D. A. Yashar, M. J. Wilson, H. R. Kopke *et al.*, "An investigation of refrigerant void fraction in horizontal, microfin tubes," *HVAC&R Res.*, vol. 7, no. 1, pp. 67–82, 2001.
[29] National Institute of Standards and Technology (NIST). (2023). Measurement and modeling of pressure drop and void fraction of R-410A in small diameter tubes. *Air-Conditioning, Heating, and Refrigeration Technology Institute.* [Online]. AHRTI Report No. 20110-01, Available: https://www.ahrinet.org/system/files/2023-08/AHRTI-Rpt-20110-01.pdf
[30] S. Komala-Sheshachala, R. Sevilla, and O. Hassan, "A coupled HDG-FV scheme for the simulation of transient inviscid compressible flows," *Comput. & Fluids*, vol. 202, 104495, 2020.
[31] A. Golijanek-Jędrzejczyk, D. Świsulski, R. Hanus *et al.*, "Uncertainty of the liquid mass flow measurement using the orifice plate," *Flow Measurement and Instrumentation*, vol. 62, pp. 84–92, 2018.
[32] M. S. Carvalho, J. C. P. de Oliveira, and J. L. de Lima, "Uncertainty analysis in flow measurement: A practical approach," *Flow Meas. Instrum.*, vol. 50, pp. 124–130, 2016.
[33] S. Che, D. Breitenmoser, Y. Y. Infimovskiy *et al.*, "CFD Simulation of two-phase flows in helical coils," *Front. Energy Res*., vol. 8, 2020.
[34] T. A. Ibrahim and M. A. M. Hassan, "Condensation heat transfer characteristics of R22, R134a, R410A and R407C on single horizontal plain and finned tubes," *Int. Rev. Mech. Eng*., vol. 7, no. 4, 2013.
[35] H. S. Wang and J. W. Rose, "A theory of film condensation in horizontal noncircular section microchannels," *J. Heat Transfer,* vol. 127, no. 10, 2005.
[36] W. S. Kuo, Y. M. Lie, Y. Y. Hsieh *et al.*, "Condensation heat transfer and pressure drop of refrigerant R-410A flow in a vertical plate heat exchanger," *Int. J. Heat Mass Transf*., vol. 48, no. 25–26, pp. 5246–5257, 2005.
[37] C. Kondou and P. Hrnjak, "Condensation from superheated vapor flow of R744 and R410A at subcritical pressures in a horizontal smooth tube," *Int. J. Heat Mass Transf*., vol. 55, no. 11–12, pp. 2779–2791, 2012.